IPEM Institute of Physics and Engineering in Medicine

ACCEPTED MANUSCRIPT

A validated Geant4 model of a whole-body PET scanner with four-layer DOI detectors

1
2
3
4
5
6
7
8
9
10
11
12
13

1 A validated Geant4 model of a whole-body PET
2 scanner with four-layer DOI detectors

3 **Abdella M. Ahmed**[1,2]**, Andrew Chacon**[1,2]**, Harley Rutherford**[1,2]**,**
4 **Go Akamatsu**[3]**, Akram Mohammadi**[3]**, Fumihiko Nishikido**[3]**,**
5 **Hideaki Tashima**[3]**, Eiji Yoshida**[3]**, Taiga Yamaya**[3]**, Daniel R.**
6 **Franklin**[4]**, Anatoly Rosenfeld**[2,5]**, Susanna Guatelli**[2,5]**, Mitra**
7 **Safavi-Naeini**[1,2,6]

8 [1] Australian Nuclear Science and Technology Organisation (ANSTO), NSW,
Australia
9
10 [2] Centre for Medical Radiation Physics, University of Wollongong, Wollongong NSW
11 2522 Australia
12 [3] National Institute of Radiological Sciences (NIRS), National Institutes for
13 Quantum and Radiological Science and Technology, 4-9-1 Anagawa, Inage-ku, Chiba
14 263-8555, Japan
15 [4] School of Electrical and Data Engineering, University of Technology Sydney,
16 Australia
17 [5] Illawarra Health and Medical Research Institute, University of Wollongong,
18 Wollongong NSW 2522 Australia
19 [6] Brain and Mind Centre, University of Sydney, Sydney, NSW, Australia

20 E-mail: abdellaa@ansto.gov.au

21 E-mail: mitras@ansto.gov.au

*A validated Geant4 model of a whole-body PET scanner with four-layer DOI detectors*2

Abstract. The purpose of this work is to develop a validated Geant4 simulation model of a whole-body prototype PET scanner constructed from the four-layer depth-of-interaction detectors developed at the National Institute of Radiological Sciences, National Institutes for Quantum and Radiological Science and Technology, Japan. The simulation model emulates the behaviour of the unique depth of interaction sensing capability of the scanner without needing to directly simulate optical photon transport in the scintillator and photodetector modules. The model was validated by evaluating and comparing performance metrics from the NEMA NU 2-2012 protocol on both the simulated and physical scanner, including spatial resolution, sensitivity, scatter fraction, noise equivalent count rates and image quality. The results show that the average sensitivities of the scanner in the field-of-view were 5.9 cps/kBq and 6.0 cps/kBq for experiment and simulation, respectively. The average spatial resolutions measured for point sources placed at several radial offsets were 5.2±0.7 mm and 5.0±0.8 mm FWHM for experiment and simulation, respectively. The peak NECR was 22.9 kcps at 7.4 kBq/mL for the experiment, while the NECR obtained via simulation was 23.3 kcps at the same activity. The scatter fractions were 44% and 41.3% for the experiment and simulation, respectively. Contrast recovery estimates performed in different regions of a simulated image quality phantom matched the experimental results with an average error of -8.7% and +3.4% for hot and cold lesions, respectively. The results demonstrate that the developed Geant4 model reliably reproduces the key NEMA NU 2-2012 performance metrics evaluated on the prototype PET scanner. A simplified version of the model is included as an advanced example in Geant4 version 10.5.

1. Introduction

Positron emission tomography (PET) is a non-invasive nuclear medicine technique that is used for the clinical diagnosis of cancer and the study of a range of diseases and biochemical processes in living organisms. The quality of reconstructed PET images is limited by the amount of activity in the object, the duration of the scan, and the performance of the PET scanner - which, in turn, depends on its constituent components, such as the type and size of scintillator material used, the detection efficiency, geometrical arrangement of the detectors and the readout electronics. In addition, the choice of parameters for data acquisition (such as acquisition time, energy window, and coincidence timing window) and reconstruction (choice of algorithm, number of subsets, number of iterations etc.) also affect the quality of the reconstructed image. Experimental optimisation of these parameters is very expensive in terms of time, materials and labour.

Monte Carlo simulation provides a versatile and low-cost alternative to experimental optimisation of imaging parameters. High-fidelity simulations of existing physical scanners, validated for correctness against experimental measurements, enable the development of new image reconstruction algorithms, segmentation methods and optimised imaging protocols for quantitative evaluation of radiotracer uptake metrics. A simulation-based approach enables quantitative imaging experiments to be planned with advance knowledge of the achievable signal to noise ratio and other signal quality

A validated Geant4 model of a whole-body PET scanner with four-layer DOI detectors 3

65 metrics, without wasting time, radiotracer and sacrificed animals on potentially futile
66 experiments [1, 2, 3, 4, 5]. This approach has the advantage of perfect repeatability -
67 for example, exactly the same spatio-temporal radiotracer uptake distribution can be
68 imaged with different scanner parameters (for example, timing and energy windows).

69   A wide range of Monte Carlo simulation platforms have been developed for this
70 purpose including the Geant4 Application for Tomographic Emission (GATE) [6, 7, 8],
71 Simulation System for Emission Tomography (SimSET) [9, 10, 11], Geant4-based
72 Architecture for Medicine-Oriented Simulations (GAMOS) [12, 13] and a PET-dedicated
73 Monte Carlo tool based on PENELOPE (PeneloPET) [14].

74   The performance of clinical PET scanners is quantified using the National Electrical
75 Manufacturers Association (NEMA) NU 2 standard, first published in 1994 and most
76 recently updated in 2012 and 2018 [15, 16, 17]. The NEMA NU 2 standard provides
77 a suite of protocols for the standardised measurement of spatial resolution, sensitivity,
78 scatter fraction, count losses and random measurements, and the accuracy of attenuation
79 and scatter correction for image quality. Many validation works for Monte Carlo models
80 of different scanners have been conducted by following the NEMA NU 2 protocols (or the
81 related NU 4 standard for preclinical scanners) on corresponding simulated and physical
82 scanners and comparing the results. Lamare et al. developed a simulation model of
83 the Philips Allegro/GEMINI PET system in GATE, and its spatial resolution, noise
84 equivalent count rate, sensitivity and scatter fraction were compared with the measured
85 results [8]. Gonias et al. compared scatter fractions obtained using the Siemens Biograph
86 mCT PET scanner and its corresponding GATE model, obtaining good agreement while
87 observing that decreasing the dead-time of the simulation improved the accuracy of the
88 simulation's scatter fraction estimate [18]. Poon et al. performed NEMA validation of
89 the scatter fraction, count rates and spatial resolution obtained using a SimSET model of
90 the same Siemens Biograph mCT scanner and compared these results with experimental
91 data [11]. Ghabrial et al. validated a GATE simulation model, also of the Siemens
92 Biograph mCT PET/CT scanner, using the NEMA NU 2 protocols, finding that the
93 spatial resolution and sensitivity obtained from the simulation tended to underestimate
94 experimental values, while scatter fraction was slightly overestimated [19].

95   The purpose of this work is to develop and validate a Geant4 simulation model of
96 the world's first whole-body prototype PET scanner constructed from 4-layer depth-of-
97 interaction (DOI) detectors developed at the National Institute of Radiological Sciences
98 (NIRS), National Institutes for Quantum and Radiological Science and Technology,
99 Japan. This scanner is specifically designed for in-beam clinical quality assurance in
100 heavy ion therapy, in which the positron-emitting radioactive fragments produced during
101 therapy are imaged in order to provide range verification information. The developed
102 model can be used by researchers to help plan and optimise imaging experiments to be
103 performed with the heavy ion beamlines at NIRS; it will also be a valuable tool to assist
104 in the design of newer versions or configurations of the scanner.

105   The use of 4-layer DOI detectors allows the prototype to achieve uniformly high
106 spatial resolution throughout the entire field of view (FOV), with excellent contrast

A validated Geant4 model of a whole-body PET scanner with four-layer DOI detectors 4

107 recovery in axially-offset regions with limited radiotracer uptake. Utilisation of DOI
108 information avoids the broadening of lines of response in the radial dimension which
109 occurs near the periphery of the scanner due to parallax error. This results in improved
110 spatial resolution in the radial direction in the reconstructed image compared to the
111 non-DOI case, at the cost of a substantially larger system matrix (by a factor of N^2 for
112 N-layer DOI). The experimental performance of the 4-layer DOI detectors have been
113 extensively evaluated by Tsuda et al. and Hirano et al. [20, 21]; the complete scanner is
114 described and analytically modelled by Tashima et al. and experimentally characterised
115 using the NEMA NU 2 protocols by Akamatsu et al. [22, 23].

116 The Geant4 Monte Carlo simulation framework was selected as the development
117 platform due to the large body of existing particle therapy simulation code available for
118 Geant4, and the ease with which this code may be integrated with the simulated PET
119 scanner for complete simulation and modelling of PET quality assurance. Additionally,
120 the model can be easily modified to incorporate other unconventional geometries (such as
121 the Single-Ring OpenPET [22]) which are optimised for particle therapy QA; simulation
122 of non-right-cylindrical geometries is not straightforward in GATE.

123 Development of a validated model for this particular scanner will be of considerable
124 value and utility in a number of different projects. The physical scanner is used for a
125 wide range of research, including inverse dose estimation methods [24, 25], evaluation
126 of Geant4 hadronic ion inelastic physics models for range verificaion in particle therapy
127 [26] and experimental evaluation of the use of positron-emitting ion beams for particle
128 therapy [27, 28]. Furthermore, an oblique-ring version of this scanner will be used
129 for clinical quality assurance work at HIMAC; the proposed Monte Carlo simulation
130 model will be useful for developing and testing the clinical quality assurance protocols
131 [29]. The developed model directly reflects the physical structure of the scanner, while
132 utilising an analytic model of the light-sharing scheme used by the unique 4-layer
133 DOI-sensing system employed in the scanner; this avoids the need to simulate optical
134 photon transport, thereby greatly improving the speed of the simulation. Simulations
135 were conducted according to the NEMA NU 2-2012 protocol‡, and spatial resolution,
136 sensitivity, scatter fraction (SF), noise equivalent count rates (NECR) and image
137 quality were evaluated. The results were validated against corresponding experimental
138 measurements obtained with the prototype PET scanner [16, 23].

139 A simplified version of the simulation model is now included as an advanced example
140 in Geant4 version 10.5.

2. Materials and Methods

142 All source code developed for this project is available via the following URL:
143 https://bitbucket.org/msafavi/whole-body-doi-pet-simulation-model.

‡ The 2018 update of the NEMA NU 2 protocol is equivalent to the 2012 version from the perspective
of the parameters evaluated in this study.

*A validated Geant4 model of a whole-body PET scanner with four-layer DOI detectors*5
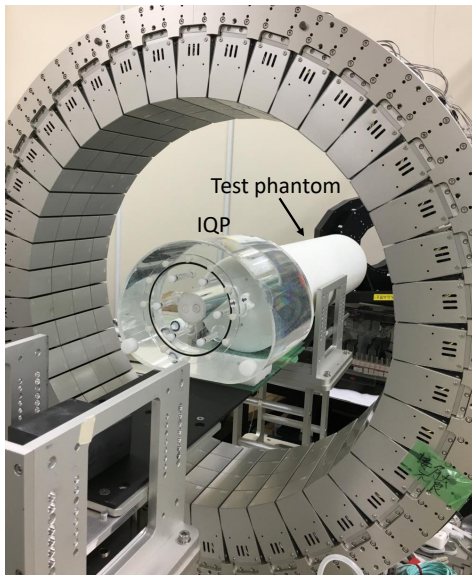
(a) Prototype scanner
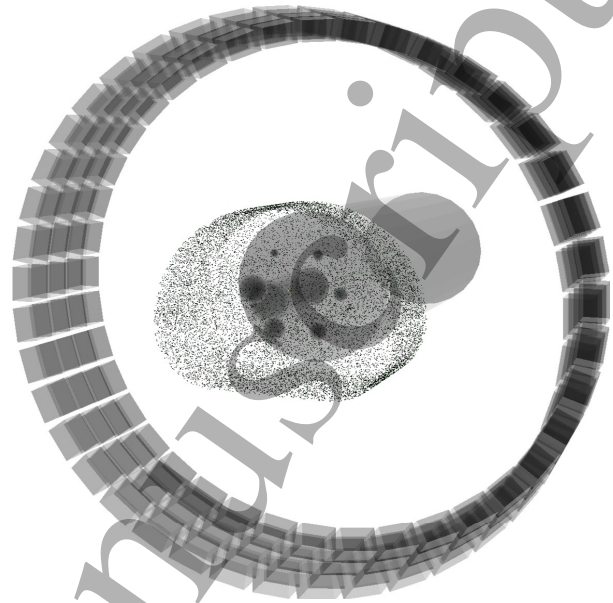
(b) Simulation

Figure 1: The whole-body DOI-PET prototype and equivalent simulation with image quality phantom (IQP) and test phantoms.

2.1. Whole-body DOI-PET design

The whole-body DOI-PET prototype being modelled in this work consists of four rings, each composed of 40 detector modules with DOI capability [23]. The physical PET scanner and its corresponding simulation model are shown in Figure 1(a) and Figure 1(b), respectively, and the scanner specifications are summarised in Table 1. The scanner has an internal diameter of 660 mm with an axial FOV of 215 mm. Each detector module consists of a $16 \times 16 \times 4$ array of Zr-doped gadolinium oxyorthosilicate (GSOZ) scintillation crystals with dimensions of $2.8 \times 2.8 \times 7.5$ mm^3, with the outermost layer of the array optically coupled to a 64-channel (8×8) flat panel position-sensitive photomultiplier tube (PS-PMT). Depth of interaction is determined using a light-sharing method in which the optical photon distributions arriving at the PS-PMT are modified via the insertion of radial reflectors in the crystal array with different patterns for each layer (see Figure 4) [21]. This results in the radial component of the 3D point of interaction being encoded in the 2D optical photon distribution histogram as the absence or presence of a translation in the axial and/or tangential direction.

2.2. Simulation Model

A schematic illustration of the PET scanner (along with the NEMA NU 2 image quality phantom) is shown in Figure 2. The scanner was simulated using Geant4 toolkit version 10.5.p01; the standard physics option 3 model (G4EmStandardPhysics_option3) was used for electromagnetic interactions [30, 31]. The simulated scanner has the same

A validated Geant4 model of a whole-body PET scanner with four-layer DOI detectors 6

Table 1: Parameters of the PET scanner

Parameter	Value
Scintillation material	GSOZ (phys) / GSO (sim)
Photodetector	64-ch (8×8) flat panel PS-PMT
Size of crystal	$2.8\times2.8\times7.5$ mm^3
Crystals per detector	$16\times16\times4$
Ring diameter	660 mm
Axial field-of-view	215 mm
Number of rings	4
Number of detectors per ring	40
Time resolution	4.4 ns

164 geometry as the physical scanner (Table 1). The scintillation material used in the
165 simulation is GSO rather than GSOZ; this is because the zirconium dopant used in the
166 prototype PET scanner is only present in trace quantities to increase the light output
167 (by around 20% compared with that of undoped GSO), and has an insignificant effect
168 on the other physical properties of the scintillator [32]. The crystal block is placed inside
169 an aluminium light shield with a thickness of 0.3 mm. A paralysable dead-time of 256 ns
170 is applied on each block. The output of the simulation is stored as single list-mode data;
171 coincidences are detected via post-simulation analysis. The coincidence timing window
172 is set to 10 ns, while the energy window is 400 keV-600 keV.

173   The list-mode coincidence data records the global crystal identification number for
174 both endpoints of each line of response.

175   To greatly increase the speed of the simulation, optical photon emission and
176 transport is not simulated; instead, the true location of any energy deposition in
177 the scintillators is logged, and the position response of the PS-PMT and Anger logic
178 decoding scheme is modelled analytically based on this location. This approach is fully
179 described in Section 2.2.2; it is similar to the approach normally used by GATE, although
180 the DOI-decoding logic is different to any of the systems supported by that simulator
181 [7].

182 *2.2.1. Detection Efficiency*   Following deposition of energy in a scintillation crystal, the
183 probability that an event is detectable depends on the scintillator light yield and emission
184 spectrum, the transfer efficiency of the scintillator-PMT system, the quantum efficiency
185 of the PMT and the detection threshold of the pulse detector. These terms do not need to
186 be individually determined in the simulation to provide an accurate model of the system
187 sensitivity. Instead, an overall detection efficiency factor for the scintillator/PMT chain
188 is estimated by performing a sensitivity measurement on the simulated scanner (based
189 on the NEMA NU 2-2012 sensitivity scan) with an axial line source at low activity (so
190 as to eliminate the impact of detector module dead-time) at the centre of the scanner

A validated Geant4 model of a whole-body PET scanner with four-layer DOI detectors 7
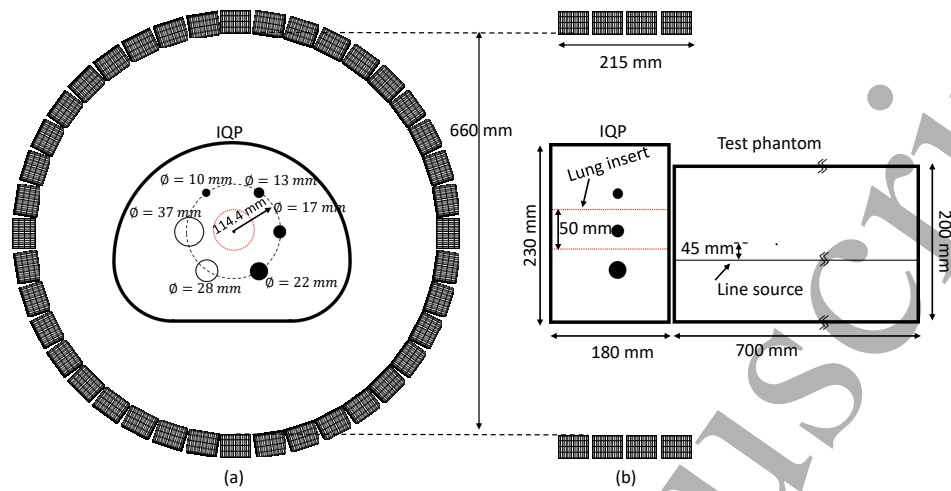

Figure 2: Schematic illustration of the PET scanner with NEMA NU2 image quality phantom (IQP). The red circle at the centre of the FOV represents the lung insert, filled black circles are "hot" lesions and those with no colour are "cold" lesions. (a) Transversal view, (b) axial view, where the test phantom is placed next to the IQP.

191 and an assumed detection probability of 100%, then reducing the proportion of detected
192 events until the mean detection count rate per unit source activity density matches the
193 experimentally observed sensitivity. This detection probability value was found to be
194 88%.

195 *2.2.2. Interaction Localisation and Error Modelling* Full simulation of optical photon
196 emission and transport is not performed due to the high computational burden that
197 this would impose. Instead, the exact amount of energy deposited and the true point of
198 interaction within a crystal for each detected event is recorded in the simulation, and
199 deliberately degraded according to a model of the pulse processing and DOI estimation
200 system implemented in the actual scanner to produce a realistic error distribution.

201 The effective energy resolutions of individual scintillator crystals in the simulation
202 are randomly generated at the start of the simulation and stored in a look-up table. This
203 per-crystal parameter combines the variations in energy resolution between the energy
204 resolution of individual scintillation crystals, optical coupling efficiencies and PMT gains
205 of a real scanner as a single Gaussian random variable representing overall effective
206 energy resolution. The mean value of this effective energy resolution was set to 15%
207 with a standard deviation of 1% (such that more than 95% of crystals had an effective
208 energy resolution between 13% and 17%); these values were based on measurements
209 obtained from the physical scanner.

210 In the physical scanner, the depth of interaction is encoded using a pattern of
211 reflectors inserted between adjacent pairs of crystals in each layer, with the pattern of
212 reflectors shifted by one crystal axially in the second layer, one crystal tangentially in
213 the third layer, and then one crystal in both dimensions in the fourth layer [20]. In

A validated Geant4 model of a whole-body PET scanner with four-layer DOI detectors 8

214 this way, the interacting layer can be determined by observing the shift of the optical
215 photon distribution observed at the base of the bottom layer, which is optically coupled
216 to a position-sensitive PMT. To simplify the electronics, the 64 anodes of the PMT
217 (Hamamatsu H9500) are combined via an Anger logic resistive ladder network to four
218 electrical outputs. If all energy is deposited in a single interaction, the interacting
219 crystal may be uniquely identified by decoding the Anger logic signals via analysis of
220 the relative pulse heights; if the energy is distributed between multiple crystals, the
221 centroid of the resulting projections is used to assign the endpoint location.

222   A simplified diagram which illustrates crystal identification and DOI quantification
223 is shown in Figure 4 for a 4-layer DOI detector with an 8×8 crystal array coupled to
224 an ideal position-sensitive PMT with Anger-logic readout at each corner (Figure 3 (a)).
225 The reflector pattern for each layer and the expected position response are shown in
226 Figure 4 (a) and Figure 4 (b), respectively. The expected position response of all layers
227 when projected in 2D histogram is shown in Figure 4 (c). The size of the pixel in which
228 the 2D position histogram was half of the crystal pitch. Crystal identification (and
229 hence DOI quantification) is performed via a mapping of the 2D position projection
230 (Figure 5 (a)) to a look-up table (Figure 5 (b)).

231   The simulation uses the following process to emulate the physical scanner's method
232 for determining the specific crystal with which a gamma photon has interacted:

233 • The spatial position P of the centre of mass of the exact locations of all energy
234   depositions in a detector block is calculated;

235 • The individual amounts of energy deposited in each crystal are scaled by a random
236   gain term according to the energy resolution of each crystal, and the weighted sum
237   E calculated;

238 • The crystal $C_{i,j,k}$ in which P is located is identified (where i, j and k are the indices
239   of the crystal's position in x, y and z dimensions);

240 • A number of optical photons N emitted from $C_{i,j,k}$ is calculated (but *not* simulated)
241   based on E and the nominal photon yield of the crystal;

242 • The exact location on the PMT surface to which the optical photons are mapped
243   due to the reflector patterns is then determined according to the 16×16×4 extension
244   of Figure 4 and 5;

245 • An empirically-derived error is added to this 2D location (iteratively optimised
246   to achieve the best overall match between the simulation and experimental spatial
247   resolutions) to model the finite signal to noise ratio of the PMT and the quantisation
248   noise resulting from digitisation of the readout signals;

249 • The result coordinates are quantised to a 32×32 grid (with resolution equal to half
250   the crystal width) and mapped back to a crystal in the scintillator array - the x
251   and y index are determined by dividing the quantised location on the grid by two
252   in each dimension, while the layer is determined by mapping the quantised location
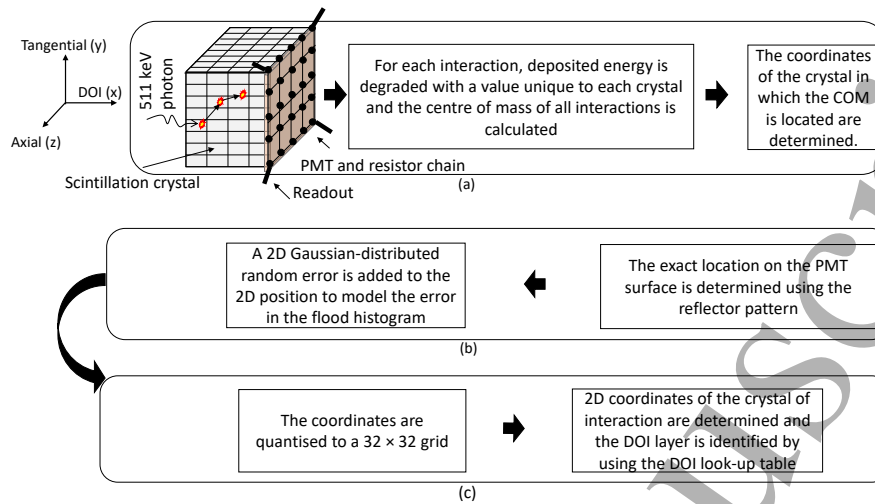253   with a DOI look-up table as shown in Figure 5.

Figure 3: Flowchart illustrating the mapping of gamma photon interactions to a specific crystal within the detector block, without simulating optical photons. (a) Identification of the crystal where the centre of mass of the interactions is located, including any inter-crystal scatter in the scintillator block; (b) modeling the imperfect position response of the light-sharing scintillators, PMT and Anger logic by adding a Gaussian-distributed 2D error optimised to best match the experimental scanner performance; and (c) identification of the crystal of interaction in 3D by using a DOI look-up table. The PMT and the resistor network are shown for illustrative purposes only.

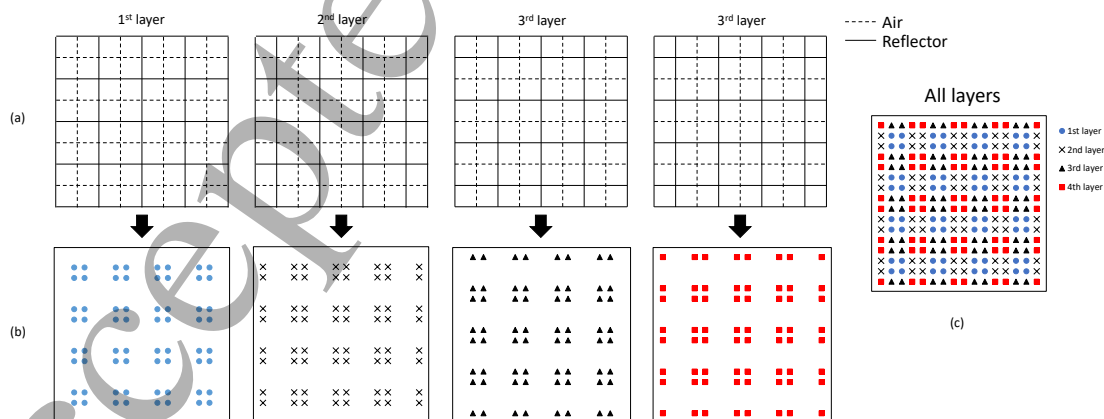

Figure 4: Illustration of position response for a four layer DOI detector with a (simplified) 8×8×4 crystal array (Figure 3 (a)). (a) Reflector pattern for each layer, (b) expected 2D position response for each layer, and (c) the overall position response when projected in a 2D position histogram. The actual 16×16×4 array follows an extension of the same pattern.

*A validated Geant4 model of a whole-body PET scanner with four-layer DOI detectors*10
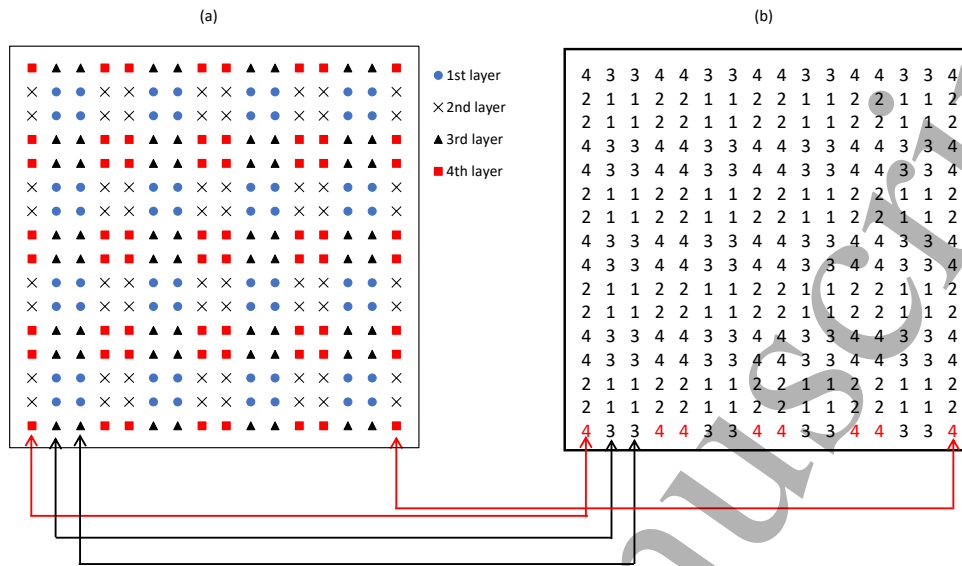

Figure 5: Mapping of the position map to DOIs via look-up table. For example, all the position responses that are at (or near) the red rectangular dots are identified as occuring in layer 4.

2.3. NEMA NU 2-2012 Performance Evaluation

Performance of the simulated scanner was evaluated according to the NEMA NU 2-2012 protocol, and compared with experimental measurements performed on the physical scanner.

2.3.1. Sensitivity Sensitivity was evaluated by modelling a 700 mm long polyethylene tube (with inner and outer diameters of 1 mm and 3 mm, respectively), filled with ^{18}F solution and inserted into between one and five concentric 700 mm long aluminium sleeves. List-mode data was recorded for 600 s at two positions within the FOV: centred (with activity ranging from 2.88 MBq to 3.85 MBq), and at a radial displacement of 100 mm (with activity ranging from 2.0 MBq to 2.67 MBq). List-mode data was rebinned using the single slice rebinning algorithm, with a slice thickness of 1.5 mm, over an axial range of 215 mm. Sensitivity was calculated as the number of true coincidence events per unit activity. The sensitivity measurement with no attenuation was extrapolated from the data set (as per the NEMA NU 2-2012 protocol).

2.3.2. Spatial Resolution Spatial resolution was evaluated by simulating a set of point-like cylindrical sources ($\oslash = h = 1$ mm) filled with ^{18}F solution. The point sources were placed at radial offsets of 10 mm, 100 mm and 200 mm, at the centre of axial FOV (AFOV) and at $\frac{3}{8}$ of the AFOV with a total source activity of 0.61 MBq. List mode data was recorded for 600 s. A 3D sinogram was generated with a maximum ring difference of 40 and then a 2D sinogram was generated by the Fourier rebinning algorithm (FORE). The images were reconstructed using filtered back projection (FBP), with a voxel size

A validated Geant4 model of a whole-body PET scanner with four-layer DOI detectors 11

275 of $1\times1\times1$ mm³. Spatial resolution was measured as the full width at half maximum
276 (FWHM) of the point source for the radial, tangential and axial directions. The spatial
277 resolution was also evaluated for an image reconstructed without DOI information, and
278 a comparison with the resolution obtained with the full 4-layer DOI reconstruction is
279 provided in Appendix A.1.

280 *2.3.3.   Noise Equivalent Count Rate and Scatter Fraction* The NECR and SF of
281 the scanner were evaluated using a cylindrical polyethylene phantom ($\oslash = 200$ mm,
282 $h = 700$ mm) with a line source inserted at a radial offset of 45 mm. The phantom was
283 positioned at the centre of the FOV, with its axis parallel to the axis of the scanner.
284 List-mode data was collected for a range of activities (422.7 MBq to 1 MBq). Randoms
285 were estimated using a delayed coincidence window method. The single slice rebinning
286 algorithm was used to form prompt and delayed-coincidence sinograms. Count rates and
287 SFs were evaluated from the sinograms and plotted as a function of effective activity
288 concentration, defined in the NEMA NU 2-2012 standard as the average source activity
289 during the acquisition divided by the phantom volume.

290 *2.3.4.   Image Quality and Contrast Recovery* A NEMA NU 2-2012 image quality
291 phantom (IQP) was modelled in Geant4 and used for the evaluation of image quality and
292 contrast recovery (CR) (DSC model PET/IEC-BODY/P with lung insert). The "warm"
293 background volume of the phantom was filled with ^{18}F, with an activity concentration
294 of 5.31 kBq/mL. Four spherical "hot" lesions with diameters of 10 mm, 13 mm, 17 mm
295 and 22 mm were filled with an activity concentration eight times greater than the
296 background. Two spherical "cold" lesions with diameters of 28 mm and 37 mm were
297 filled with non-radioactive water. A line source containing 72.1 MBq of ^{18}F was inserted
298 into a cylindrical polyethylene phantom and positioned axially adjacent to the IQP to
299 simulate background activity from outside of the FOV as shown in Figure 2.

300   Images were reconstructed using 3D ordinary-Poisson ordered-subset expectation-
301 maximisation (OSEM) with 4 iterations and 8 subsets. Projection data was generated by
302 forward projection using a system matrix in which the detector response was modelled
303 using a simple Gaussian function [33]. The number of image voxels was $125\times125\times150$,
304 with a voxel size of $3.0\times3.0\times3.0$ mm³. A 6 mm FWHM Gaussian filter was applied to the
305 reconstructed image. Random correction was performed using the delayed coincidence
306 method. Attenuation correction factors were calculated directly based on knowledge of
307 the phantom composition. Component-based normalisation was used, and single scatter
308 simulation was applied to perform scatter correction.

309   The CR and background variability were also evaluated for an image reconstructed
310 without DOI information, and a comparison with the results obtained using the full
311 4-layer DOI reconstruction is provided in Appendix A.2.

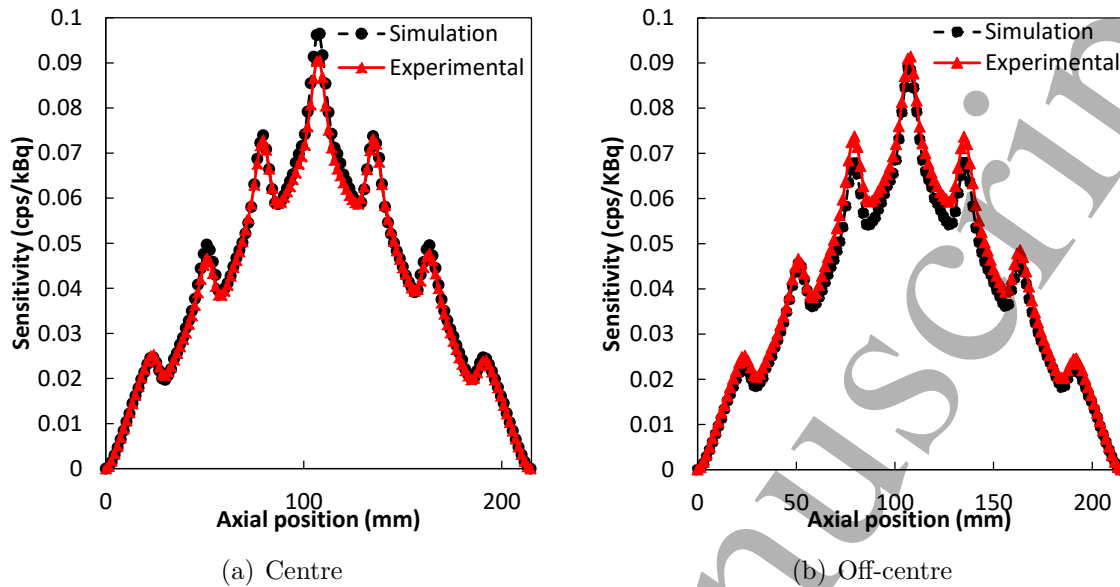*A validated Geant4 model of a whole-body PET scanner with four-layer DOI detectors* 12

Figure 6: Axial sensitivity profile of the line source in both evaluated positions.

(a) Centre   (b) Off-centre

3. Results

3.1. Sensitivity

The axial sensitivity profiles from the simulation are shown together with the corresponding experimental measurements (previously reported in [23]) in Figure 6. The system sensitivities for the experiment and simulation at the centre of the FOV were 5.9 cps/kBq and 6.2 cps/kBq, respectively, and the sensitivities at 10 cm radial offset were 5.9 cps/kBq and 5.7 cps/kBq for the experiment and simulation, respectively. The physical scanner exhibits the same sensitivity at both locations, whereas sensitivity is slightly higher at the centre in the simulation.

3.2. Spatial Resolution

The values of the spatial resolution for the simulation are summarised in Table 2, together with the previously reported experimental values for the physical scanner. The average spatial resolutions of the simulation and experiment were 5.0±0.8 mm and 5.2±0.7 mm, respectively.

3.3. Noise Equivalent Count Rate and Scatter Fraction

The count rate and the SF profiles of the simulated scanner are shown in Figure 7 and Figure 8, respectively, together with the experimental results from the physical scanner. The simulation and the experimental profiles are in close agreement except at high activity, where the counts significantly decrease in the case of experiment. The maximum NECR and SF for the experiment were 22.9 kcps and 48.4%, respectively, at

A validated Geant4 model of a whole-body PET scanner with four-layer DOI detectors 13

Table 2: Spatial resolution for the simulated and physical scanners.

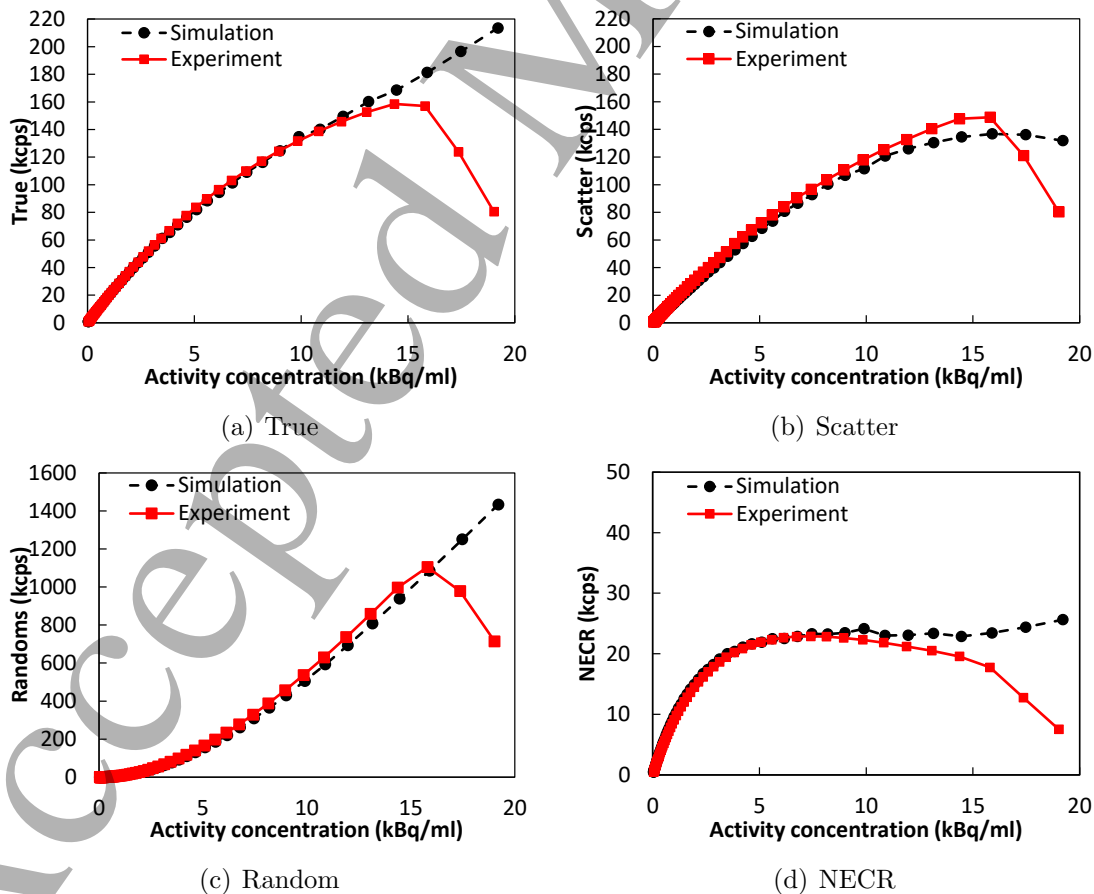| Dimension	Offset (mm)	Sim.	Phys.	Difference (%)
Radial	10	4.0	4.1	2.8
	100	5.1	4.8	-7.2
	200	6.4	5.9	-8.8
Tangential	10	4.0	4.8	+16.3
	100	4.1	4.7	+13.7
	200	4.6	4.8	+4.0
Axial	10	5.9	6.5	+9.6
	100	5.1	5.7	+9.7
	200	5.4	5.8	+6.0

(a) True

(b) Scatter

(c) Random

(d) NECR

Figure 7: Count rates of the whole-body PET scanner for the simulation and physical scanner.

A validated Geant4 model of a whole-body PET scanner with four-layer DOI detectors 14
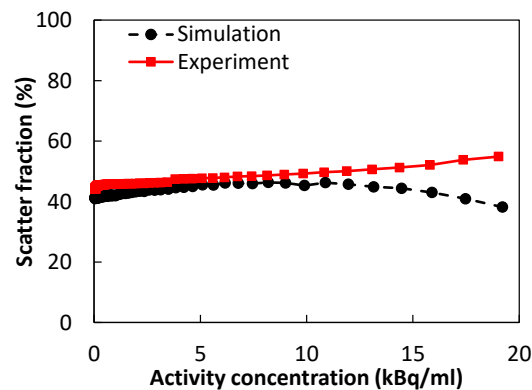
Figure 8: Scatter fraction profiles for the simulation and physical scanner.

(a) Simulation   (b) Experiment
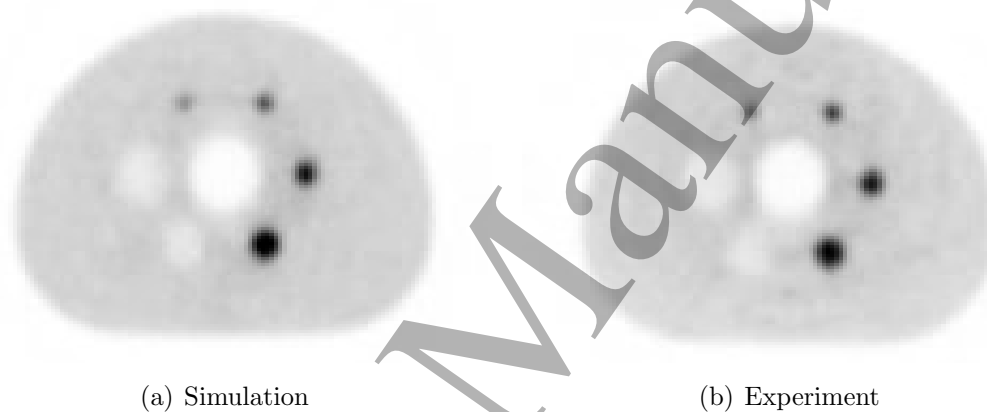
Figure 9: Reconstructed images of the image quality phantom.

an activity concentration of 7.45 kBq/mL. The NECR curve for the simulation does not peak at a specific activity. The NECR and SF of the simulation at the peak activity of the experiment (7.45 kBq/mL) were 23.3 kcps and 46.0%, respectively. The SF of the experiment and simulation at low activity (0.04 kBq/mL) were 44.0% and 41.3%, respectively.

3.4. Image Quality and Contrast Recovery

The reconstructed images of the IQP phantom are shown in Figure 9. The CR and background variability of the IQP for the simulated and physical scanners are listed in Table 3; the results are in close agreement. The average residual of the lung insert for a 30 mm region-of-interest (ROI) for the simulation was 5.4% compared to the experimental value of 9.1%.

4. Discussion

The main objective of this work was to develop and validate a simulation model of the world's first 4-layer DOI-enabled whole-body prototype PET scanner developed at the

*A validated Geant4 model of a whole-body PET scanner with four-layer DOI detectors*15

Table 3: Comparison of contrast recovery and background variability.

ROI ⌀ (mm)	Contrast (%)		Background variability (%)	
	Sim.	Phys.	Sim.	Phys.
10(h)	16.0	20.7	5.4	9.2
13(h)	27.2	31.1	5.1	8.9
17(h)	37.9	40.6	4.7	8.4
22(h)	46.4	43.3	4.2	7.9
28(c)	34.2	33.2	3.9	7.4
37(c)	41.4	39.9	3.6	7.0

346 NIRS-QST, Japan.

347   The simulation demonstrated slightly higher sensitivity compared to the physical
348 scanner at the centre of the FOV, as shown in Figure 6(a). The difference could be
349 due to experimental error in the placement of the source. The absolute difference in
350 sensitivity was 4.5% at the centre of the FOV and 4.1% at a radial offset of 10 cm,
351 indicating close agreement between the experiment and simulation.

352   The average magnitude of the error between the spatial resolutions obtained in
353 the simulation and experiment was 5.1%, which also shows a close agreement. The
354 small error could be due to the assumption of a linear response shift of the PMT due
355 to the reflector model being overly simplistic. Developing a more accurate look-up
356 table based on a full optical photon simulation of a detector block will provide a more
357 realistic model of the behaviour of this component. Finally, errors due to positioning of
358 the point sources in the physical scanner during the experimental measurements could
359 also contribute to the discrepancies in spatial resolution; however, it is noted that the
360 discrepancy between the simulation and experimental spatial resolution is quite small
361 compared to those previously reported in validation work on other PET scanners [11, 19].

362   All the count rate performances were in a close agreement except at the highest
363 activities, where the physical scanner exhibits detector saturation as seen in Figure 7.
364 The count rate errors between experiment and simulation were 0.8% for true, 4.1% for
365 scatter, 5.9% for random and 1.8% for NECR at an activity concentration of 7.4 kBq/mL
366 (where the peak NECR occurred for the physical scanner). A maximum NECR was not
367 observed in the case of the simulation although a paralysable dead-time was applied on
368 each block detector. This may be due to the idealised data scoring scheme used in the
369 simulation in which the detectors continue accepting events without being dependent on
370 factors such as limited bandwidth for data acquisition. In practice, the highest evaluated
371 count rates do not occur in the application for which this scanner was designed (particle
372 therapy quality assurance and related research), therefore the discrepancy in this region
373 is not a major problem.

374   For the IQP (see Figure 9 and Table 3), the CR showed close agreement between the

A validated Geant4 model of a whole-body PET scanner with four-layer DOI detectors 16

375 simulated and physical scanners. The average error in CR for the hot regions was -8.7%
376 while for the cold regions it was +3.4%. The discrepancies observed in the background
377 values are more substantial, with a consistent underestimation in the simulation (-44%
378 for hot lesions and -48% for cold). This may be evidence of a background noise or error
379 contribution (for example, noise in the experimental normalisation data or detector
380 degradation) which is not currently included in the simulation and will be subject to
381 future investigation.

382 The experimental NEMA NU 2 performance evaluation data used to validate the
383 simulation model was acquired with the whole-body DOI PET scanner in the right
384 cylindrical geometry (i.e. flat configuration) as shown in Figure 1(a). However, one of
385 the unique characteristics of this scanner is that it can be mechanically reconfigured
386 into an oblique-ring geometry to enable beam access for in-beam PET imaging.
387 With the validation successfully completed, the simulation can now be extended to
388 model the oblique-ring configuration as well, which will enable accurate simulation-
389 based evaluation of clinical dose quantification and quality assurance algorithms to be
390 performed.

391 To model readout bandwidth saturation at high activities, a saturation point
392 (which, in this study, occurs at an activity concentration of 15.9 kBq/mL) can be
393 identified and a count loss model can be incorporated based on an empirical fit obtained
394 from experimental results (since several contributing factors in the data acquisition chain
395 may account for the observed saturation). This will require more measurements to be
396 performed on the real (physical) PET scanner and is the subject of ongoing experimental
397 and simulation work.

5. Conclusion

399 A Geant4 model of a whole-body prototype PET scanner constructed from the four-layer
400 DOI detector modules was validated against the experimental results obtained from the
401 physical scanner, using a range of scanner performance metrics from the NEMA NU 2
402 2012 protocol. The sensitivities of the experiment and the simulation within the FOV
403 showed an excellent agreement, with an average error of 4.3%. The spatial resolutions
404 of the simulation and the experiment were also in close agreement with average absolute
405 error of 5.1%. Count rate measurements closely matched the experimental values, except
406 at very high activities, where the count-rate limitations of the physical scanner result
407 in saturation. The peak NECR obtained with the physical scanner was 22.9 kcps at
408 an activity concentration of 7.4 kBq/mL, while it was 23.3 kcps for the simulation
409 at the same activity concentration. The contrast recovery and background variability
410 of the IQP also showed a close agreement with that of the experiment. Some of the
411 differences between the experiment and simulation could be mitigated by incorporating
412 more parameters of the prototype PET scanner into the Geant4 model.

A validated Geant4 model of a whole-body PET scanner with four-layer DOI detectors 17

6. Acknowledgements

Appendix A. Effect of DOI Information on Imaging Performance

Appendix A.1. Spatial Resolution

The spatial resolution of the scanner evaluated with and without incorporation of DOI information is given in Table A1 and Figure A1. The non-DOI results are obtained by collapsing the depths obtained in the DOI simulation to a single depth corresponding to the centroid of each 1×4 crystal column.

The radial spatial resolution of the simulation at 100 mm and 200 mm was degraded by 39.3 % and 92.5%, respectively, and that obtained in the experimental measurement was degraded at these depths by 44.2 and 94.4%, respectively, as shown in Figure A1(a). This demonstrates the value of using DOI-sensitive detectors to improve the spatial resolution of the scanner at the periphery of the FOV. Tangential and axial spatial resolution are degraded by a much smaller amount by the loss of DOI information compared to radial spatial resolution.

Appendix A.2. Image Quality

The contrast recovery (CR) coefficient obtained using the IQP with and without the use of DOI informiation is given Table A2 and Figure A2(a), and background variability is
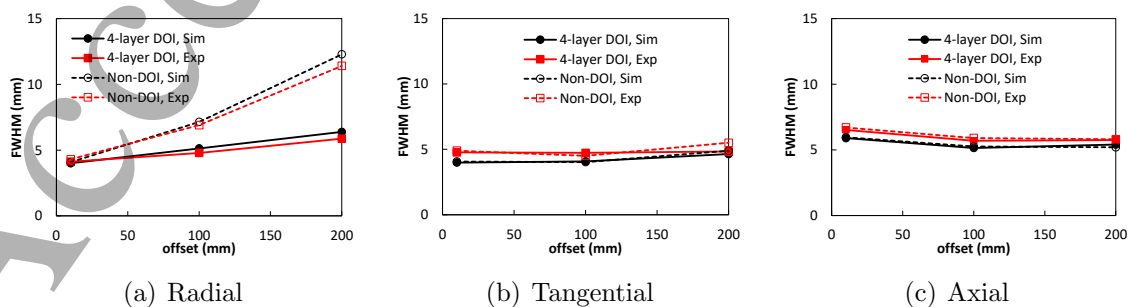

(a) Radial (b) Tangential (c) Axial

Figure A1: Spatial resolution with and without DOI information.

*A validated Geant4 model of a whole-body PET scanner with four-layer DOI detectors*18

Table A1: Spatial resolution obtained from images reconstructed with and without DOI information.

Direction	Offset (mm)	Sim (%)		Phys.		Difference (%)	
		4-layer DOI	Non-DOI	4-layer DOI	non-DOI	4-layer DOI	Non-DOI
Radial	10	4.0	4.1	4.1	4.3	+2.8	+5.0
	100	5.1	7.1	4.8	6.9	-7.2	-3.6
	200	6.4	12.3	5.9	11.4	-8.8	-7.8
Tangential	10	4.0	4.1	4.8	4.9	+16.3	+16.9
	100	4.1	4.0	4.7	4.5	+13.7	+10.6
	200	4.6	4.9	4.8	5.5	+4.0	+11.1
Axial	10	5.9	6.0	6.5	6.7	+9.6	+11.1
	100	5.1	5.3	5.7	5.9	+9.7	+10.9
	200	5.4	5.2	5.8	5.8	+6.0	+10.4

Table A2: Contrast recovery obtained with and without the use of DOI information.

ROI $\oslash$ (mm)	Sim.		Phys.	
	4-layer DOI	Non-DOI	4-layer DOI	Non-DOI
10(h)	16.0	15.8	20.7	19.8
13(h)	27.2	26.7	31.1	30.6
17(h)	37.9	37.1	40.6	39.0
22(h)	46.4	45.4	43.3	42.0
28(c)	34.2	34.6	33.2	37.1
37(c)	41.4	41.7	39.9	42.3

440 given in Table A3 and Figure A2(b). The CR and background variability values with
441 and without DOI information only exhibit small differences. This is because the spheres
442 used for this measurement are located at the centre of axial FOV.

A validated Geant4 model of a whole-body PET scanner with four-layer DOI detectors 19

Table A3: Background variability obtained with and without the use of DOI information.

ROI ⊘ (mm)	Sim.		Phys.	
	4-layer DOI	Non-DOI	4-layer DOI	Non-DOI
10(h)	5.4	5.1	9.2	10.1
13(h)	5.1	4.9	8.9	9.8
17(h)	4.7	4.4	8.4	9.3
22(h)	4.2	4.1	7.9	8.6
28(c)	3.9	3.8	7.4	8.1
37(c)	3.6	3.5	7.0	7.6

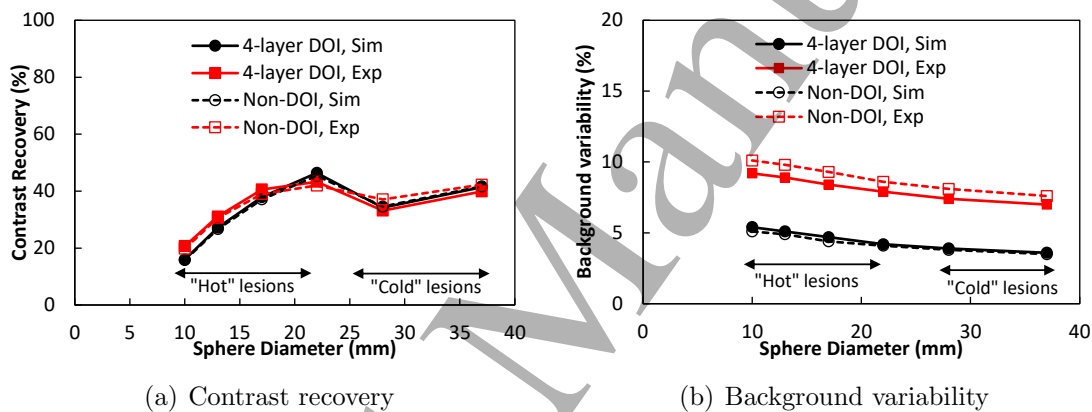(a) Contrast recovery

(b) Background variability

Figure A2: Contrast recovery and background variability for simulated and physical PET scanners, with and without the use of DOI effect.

References

[1] R. E. Schmitz, R. L. Harrison, C. W. Stearns, T. K. Lewellen, P. E. Kinahan, Optimization of noise equivalent count rate performance for a partially collimated pet scanner by varying the number of septa, IEEE Transactions on Medical Imaging 26 (2007) 935–944. doi:10.1109/TMI.2007.895485.

[2] S. Stute, T. Carlier, K. Cristina, C. Noblet, A. Martineau, B. Hutton, L. Barnden, I. Buvat, Monte carlo simulations of clinical pet and spect scans: impact of the input data on the simulated images, Physics in Medicine and Biology 56 (19) (2011) 6441–6457. doi:10.1088/0031-9155/56/19/017.
URL https://doi.org/10.1088/0031-9155/56/19/017

[3] L. Lu, H. Zhang, Z. Bian, J. Ma, Q. Feng, W. Chen, Validation of a Monte Carlo simulation of the Inveon PET scanner using GATE, Nuclear Instruments and Methods in Physics Research Section A: Accelerators, Spectrometers, Detectors and Associated Equipment 828 (2016) 170–175. doi:10.1016/j.nima.2016.04.059.
URL https://doi.org/10.1016/j.nima.2016.04.059

[4] J. E. Gillam, M. Rafecas, Monte-carlo simulations and image reconstruction for novel imaging scenarios in emission tomography, Nuclear Instruments and Methods in Physics Research Section A: Accelerators, Spectrometers, Detectors and Associated Equipment 809 (2016) 76–88. doi:10.1016/j.nima.2015.09.084.

*A validated Geant4 model of a whole-body PET scanner with four-layer DOI detectors*20

URL https://doi.org/10.1016/j.nima.2015.09.084

[5] E. Pfaehler, J. R. D. Jong, R. A. J. O. Dierckx, F. H. P. van Velden, R. Boellaard, SMART (SiMulAtion and ReconsTruction) PET: an efficient PET simulation-reconstruction tool, EJNMMI Physics 5 (1). doi:10.1186/s40658-018-0215-x.
URL https://doi.org/10.1186/s40658-018-0215-x

[6] S. Jan, G. Santin, D. Strul, S. Staelens, K. Assié, D. Autret, S. Avner, R. Barbier, M. Bardiès, P. M. Bloomfield, D. Brasse, V. Breton, P. Bruyndonckx, I. Buvat, A. F. Chatziioannou, Y. Choi, Y. H. Chung, C. Comtat, D. Donnarieix, L. Ferrer, S. J. Glick, C. J. Groiselle, D. Guez, P.-F. Honore, S. Kerhoas-Cavata, A. S. Kirov, V. Kohli, M. Koole, M. Krieguer, D. J. van der Laan, F. Lamare, G. Largeron, C. Lartizien, D. Lazaro, M. C. Maas, L. Maigne, F. Mayet, F. Melot, C. Merheb, E. Pennacchio, J. Perez, U. Pietrzyk, F. R. Rannou, M. Rey, D. R. Schaart, C. R. Schmidtlein, L. Simon, T. Y. Song, J.-M. Vieira, D. Visvikis, R. V. de Walle, E. Wiers, C. Morel, GATE: a simulation toolkit for PET and SPECT, Physics in Medicine and Biology 49 (19) (2004) 4543–4561. doi:10.1088/0031-9155/49/19/007.
URL https://doi.org/10.1088/0031-9155/49/19/007

[7] S. Jan, D. Benoit, E. Becheva, T. Carlier, F. Cassol, P. Descourt, T. Frisson, L. Grevillot, L. Guigues, L. Maigne, C. Morel, Y. Perrot, N. Rehfeld, D. Sarrut, D. R. Schaart, S. Stute, U. Pietrzyk, D. Visvikis, N. Zahra, I. Buvat, GATE v6: a major enhancement of the GATE simulation platform enabling modelling of CT and radiotherapy, Physics in Medicine and Biology 56 (4) (2011) 881–901. doi:10.1088/0031-9155/56/4/001.
URL https://doi.org/10.1088/0031-9155/56/4/001

[8] F. Lamare, A. Turzo, Y. Bizais, C. C. L. Rest, D. Visvikis, Validation of a monte carlo simulation of the philips allegro/GEMINI PET systems using GATE, Physics in Medicine and Biology 51 (4) (2006) 943–962. doi:10.1088/0031-9155/51/4/013.
URL https://doi.org/10.1088/0031-9155/51/4/013

[9] R. L. Harrison, T. K. Lewellen, The simset program, in: Monte Carlo Calculations in Nuclear Medicine, Second Edition: Applications in Diagnostic Imaging, Taylor and Francis Group, 2013.

[10] R. L. Harrison, S. B. Gillispie, T. K. Lewellen, Design and implementation of a block detector simulation in SimSET, in: 2006 IEEE Nuclear Science Symposium Conference Record, IEEE, 2006, pp. 3151–3153. doi:10.1109/nssmic.2006.356543.
URL https://doi.org/10.1109/nssmic.2006.356543

[11] J. K. Poon, M. L. Dahlbom, M. E. Casey, J. Qi, S. R. Cherry, R. D. Badawi, Validation of the SimSET simulation package for modeling the Siemens Biograph mCT PET scanner, Physics in Medicine and Biology 60 (3) (2015) N35–N45. doi:10.1088/0031-9155/60/3/n35.
URL https://doi.org/10.1088/0031-9155/60/3/n35

[12] M. Cañadas, P. Arce, P. R. Mendes, Validation of a small-animal PET simulation using GAMOS: a GEANT4-based framework, Physics in Medicine and Biology 56 (1) (2010) 273–288. doi:10.1088/0031-9155/56/1/016.
URL https://doi.org/10.1088/0031-9155/56/1/016

[13] P. Arce, J. I. Lagares, L. Harkness, D. Pérez-Astudillo, M. Cañadas, P. Rato, M. de Prado, Y. Abreu, G. de Lorenzo, M. Kolstein, A. Díaz, Gamos: A framework to do geant4 simulations in different physics fields with an user-friendly interface, Nuclear Instruments and Methods in Physics Research Section A: Accelerators, Spectrometers, Detectors and Associated Equipment 735 (2014) 304–313. doi:10.1016/j.nima.2013.09.036.
URL https://doi.org/10.1016/j.nima.2013.09.036

[14] S. España, J. L. Herraiz, E. Vicente, J. J. Vaquero, M. Desco, J. M. Udias, PeneloPET, a monte carlo PET simulation tool based on PENELOPE: features and validation, Physics in Medicine and Biology 54 (6) (2009) 1723–1742. doi:10.1088/0031-9155/54/6/021.
URL https://doi.org/10.1088/0031-9155/54/6/021

[15] NEMA Standards Publication NU 2-1994: Performance measurements of positron emission tomographs, Washington DC, USA: National Electrical Manufacturers Association (NEMA),

A validated Geant4 model of a whole-body PET scanner with four-layer DOI detectors 21

2012.

[16] NEMA Standards Publication NU 2-2012: Performance measurements of positron emission tomographs, Rosslyn, USA: National Electrical Manufacturers Association (NEMA), 2012.

[17] NEMA Standards Publication NU 2-2018: Performance measurements of positron emission tomographs, Rosslyn USA: National Electrical Manufacturers Association (NEMA), 2018.

[18] P. Gonias, N. Bertsekas, N. Karakatsanis, G. Saatsakis, A. Gaitanis, D. Nikolopoulos, G. Loudos, L. Papaspyrou, N. Sakellios, X. Tsantilas, A. Daskalakis, P. Liaparinos, K. Nikita, A. Louizi, D. Cavouras, I. Kandarakis, G. Panayiotakis, Validation of a gate model for the simulation of the siemens biograph^{TM} 6 PET scanner, Nuclear Instruments and Methods in Physics Research Section A: Accelerators, Spectrometers, Detectors and Associated Equipment 571 (1-2) (2007) 263–266. doi:10.1016/j.nima.2006.10.078.
URL https://doi.org/10.1016/j.nima.2006.10.078

[19] A. Ghabrial, D. Franklin, H. Zaidi, A monte carlo simulation study of the impact of novel scintillation crystals on performance characteristics of pet scanners, Physica Medica 50 (2018) 37–45. doi:10.1016/j.ejmp.2018.05.010.
URL https://doi.org/10.1016/j.ejmp.2018.05.010

[20] T. Tsuda, H. Murayama, K. Kitamura, T. Yamaya, E. Yoshida, T. Omura, H. Kawai, N. Inadama, N. Orita, A four-layer depth of interaction detector block for small animal pet, IEEE Transactions on Nuclear Science 51 (5) (2004) 2537–2542. doi:10.1109/tns.2004.835739.
URL https://doi.org/10.1109/tns.2004.835739

[21] Y. Hirano, M. Nitta, N. Inadama, F. Nishikido, E. Yoshida, H. Murayama, T. Yamaya, Performance evaluation of a depth-of-interaction detector by use of position-sensitive PMT with a super-bialkali photocathode, Radiological Physics and Technology 7 (1) (2013) 57–66. doi:10.1007/s12194-013-0231-4.
URL https://doi.org/10.1007/s12194-013-0231-4

[22] H. Tashima, T. Yamaya, E. Yoshida, S. Kinouchi, M. Watanabe, E. Tanaka, A single-ring OpenPET enabling PET imaging during radiotherapy, Physics in Medicine and Biology 57 (14) (2012) 4705–4718. doi:10.1088/0031-9155/57/14/4705.
URL https://doi.org/10.1088/0031-9155/57/14/4705

[23] G. Akamatsu, H. Tashima, Y. Iwao, H. Wakizaka, T. Maeda, A. Mohammadi, S. Takyu, M. Nitta, F. Nishikido, H. Rutherford, A. Chacon, M. Safavi-Naeini, E. Yoshida, T. Yamaya, Performance evaluation of a whole-body prototype PET scanner with four-layer DOI detectors, Physics in Medicine and Biologydoi:10.1088/1361-6560/ab18b2.
URL https://doi.org/10.1088/1361-6560/ab18b2

[24] T. Hofmann, M. Pinto, A. Mohammadi, M. Nitta, F. Nishikido, Y. Iwao, H. Tashima, E. Yoshida, A. Chacon, M. Safavi-Naeini, A. Rosenfeld, T. Yamaya, K. Parodi, Dose reconstruction from PET images in carbon ion therapy: a deconvolution approach, Physics in Medicine & Biology 64 (2) (2019) 025011. doi:10.1088/1361-6560/aaf676.
URL https://doi.org/10.1088/1361-6560/aaf676

[25] T. Hofmann, A. Fochi, K. Parodi, M. Pinto, Prediction of positron emitter distributions for range monitoring in carbon ion therapy: an analytical approach, Physics in Medicine & Biologydoi:10.1088/1361-6560/ab17f9.
URL https://doi.org/10.1088/1361-6560/ab17f9

[26] A. Chacon, S. Guatelli, H. Rutherford, D. Bolst, A. Mohammadi, A. Ahmed, M. Nitta, F. Nishikido, Y. Iwao, H. Tashima, E. Yoshida, G. Akamatsu, S. Takyu, A. Kitagawa, T. Hofmann, M. Pinto, D. R. Franklin, K. Parodi, T. Yamaya, A. Rosenfeld, M. Safavi-Naeini, Comparative study of alternative geant4 hadronic ion inelastic physics models for prediction of positron-emitting radionuclide production in carbon and oxygen ion therapy, Physics in Medicine & Biology 64 (15) (2019) 155014. doi:10.1088/1361-6560/ab2752.
URL https://doi.org/10.1088/1361-6560/ab2752

[27] A. Chacon, M. Safavi-Naeini, D. Bolst, S. Guatelli, D. R. Franklin, Y. Iwao, G. Akamatsu,

563   H. Tashima, E. Yoshida, F. Nishikido, et al., Monte carlo investigation of the characteristics
564   of radioactive beams for heavy ion therapy, Scientific reports 9 (1) (2019) 6537.

565 [28] A. Chacon, B. James, L. Tran, S. Guatelli, L. Chartier, D. Prokopovich, D. Franklin,
566   A. Mohammadi, F. Nishikido, Y. Iwao, G. Akamatsu, S. Takyu, H. Tashima, T. Yamaya,
567   K. Parodi, A. Rosenfeld, M. Safavi-Naeini, Experimental investigation of the characteristics
568   of radioactive beams for heavy ion therapy, Medical Physics.

569 [29] T. Yamaya, H. Tashima, OpenPET enabling PET imaging during radiotherapy, in: Personalized
570   Pathway-Activated Systems Imaging in Oncology, Springer Singapore, 2017, pp. 55–84.
571   doi:10.1007/978-981-10-3349-0_4.
572   URL https://doi.org/10.1007/978-981-10-3349-0_4

573 [30] S. Agostinelli, J. Allison, K. Amako, J. Apostolakis, et al., Geant4—a simulation toolkit, Nuclear
574   Instruments and Methods in Physics Research Section A: Accelerators, Spectrometers, Detectors
575   and Associated Equipment 506 (3) (2003) 250–303. doi:10.1016/s0168-9002(03)01368-8.
576   URL https://doi.org/10.1016/s0168-9002(03)01368-8

577 [31] J. Allison, K. Amako, J. Apostolakis, et al., Recent developments in Geant4, Nuclear Instruments
578   and Methods in Physics Research Section A: Accelerators, Spectrometers, Detectors and
579   Associated Equipment 835 (2016) 186–225. doi:10.1016/j.nima.2016.06.125.
580   URL https://doi.org/10.1016/j.nima.2016.06.125

581 [32] N. Shimura, M. Kamada, A. Gunji, S. Yamana, T. Usui, K. Kurashige, H. Ishibashi,
582   N. Senguttuvan, S. Shimizu, K. Sumiya, H. Murayama, Zr doped GSO:ce single crystals and
583   their scintillation performance, IEEE Transactions on Nuclear Science 53 (5) (2006) 2519–2522.
584   doi:10.1109/tns.2006.876006.
585   URL https://doi.org/10.1109/tns.2006.876006

586 [33] S. Kinouchi, T. Yamaya, E. Yoshida, H. Tashima, H. Kudo, H. Haneishi, M. Suga, Gpu-based
587   pet image reconstruction using an accurate geometrical system model, IEEE Transactions on
588   Nuclear Science 59 (5) (2012) 1977–1983. doi:10.1109/tns.2012.2201953.
589   URL https://doi.org/10.1109/tns.2012.2201953